

Revisiting KELT-19Ab, WASP-156b and WASP-121b in the TESS Era

FAN YANG,^{1,2,3,4} RANGA-RAM CHARY,² AND JI-FENG LIU^{3,4}

¹*Department of Astronomy, Beijing Normal University, Beijing 100875, People's Republic of China*

²*IPAC, Caltech, KS 314-6, Pasadena, CA 91125, USA*

³*National Astronomical Observatories, Chinese Academy of Sciences,
 20A Datun Road, Chaoyang District, Beijing 100101, China*

⁴*School of Astronomy and Space Science, University of Chinese Academy of Sciences, Beijing 100049, China*

(Dated: April 2019)

ABSTRACT

The relative depth of exoplanet transits in the light curve of a star at different wavelength bands can reveal the composition of the exoplanets' atmosphere. We present a re-analysis of transit depths of KELT-19Ab, WASP-156b, and WASP-121b, including data from the Transiting Exoplanet Survey Satellite (TESS). The large $\sim 21''$ TESS pixels and point spread function results in significant contamination of the stellar flux by nearby objects. We use Gaia data to fit for and remove this contribution, providing general-purpose software for this correction. We find all the three sources have a larger inclination, compared to earlier work. For WASP-121b, we find significantly smaller values (13.5 degrees) of the inclination when using the 30 minutes cadence data compared to the 2 minutes cadence data. We demonstrate using a simulation that 30-minute binning data in general, yields a smaller inclination than the true input value at 25σ . Also, we find that inclination and semi-major axis are biased small when applying a larger sampling time interval which is particularly important for deriving sub-percent transit differences between bands. If we constrain the inclination to previous work, we find the radius ratio of exoplanet to star (R_p/R_*) in the broad TESS band is 3.5σ smaller than previous work for KELT-19Ab, and consistent to within $\sim 2\sigma$ for WASP-156b and WASP-121b. The result for KELT-19Ab favors a haze-dominated atmosphere. We do not find statistically significant evidence for the $\sim 0.95\mu\text{m}$ water feature contaminating the transit depths in the TESS band for these stars but show that with photometric precision of 500ppm and with sampling of about 200 observations across the entire transit, this feature could be detectable in a more narrow z -band. Furthermore, we find that with the inclusion of the TESS photometry, WASP-121b can be fitted just as well with a cloud-free atmosphere with water vapor as with an opaque featureless model.

Keywords: planets and satellites: atmospheres—planets and satellites: gaseous planets—planets and satellites: composition—planets and satellites: individual (KELT-19Ab, WASP-156b, WASP-121b)

1. INTRODUCTION

Exoplanet transit depths in multiple bands in the light curve of a star provide clues into understanding the atmospheric composition of the exoplanet (Vidal-Madjar et al. 2003; Sing et al. 2011; Berta et al. 2012). The transmission spectrum leads to the detection of certain atomic and molecular species, as well as haze and clouds in the planet atmosphere (Seager & Deming 2010). For instance, the transit spectrum of HD 209458b and XO-1b (Deming et al. 2013) provides evidence for water and sodium absorption (Deming

et al. 2013), while Sing et al. (2016) found evidence for water vapor in hot Jupiters. Similarly, WASP-12b has been characterized as a prototypical hot Jupiter with a high C/O ratio and significant presence of aerosols in its atmosphere (Madhusudhan et al. 2011; Sing et al. 2011). However, many of these analyses rely on *Hubble* Space Telescope spectroscopy. *Hubble* due to its 90 min orbit, and passage through the South Atlantic Anomaly does not provide a good sampling of the light curve during ingress and egress. Those data are crucial for constraining the inclination of the orbit and thereby the relative transit depths in different bands.

The recently commissioned Transiting Exoplanet Survey Satellite (Ricker et al. 2015a, TESS) offers high precision photometric measurements in a broad optical band (0.6 –

$1\mu\text{m}$) that is redward of the band used by *Kepler*. TESS aims to discover transiting exoplanets around the brightest stars in the vicinity of the Sun. It has four cameras with a total field of view 24×96 degrees. The 50% ensquared-energy (within a square) half-width is 1 detector pixel or 21 arcseconds. The 90% ensquared-energy half-width is 2x2 pixels. TESS produces multi-frame images at a cadence of 30 minutes with a baseline of at least 27 days and thus does not suffer from gaps in the light curve like *Hubble*. The photometric precision is about 1% sensitivity at 16th mag.

Here we present a re-analysis of the exoplanets KELT-19Ab, WASP-156b, and WASP-121b by combining TESS with other past observations. This paper is organized as follows. Section 2 describes the generation of TESS light curves, derivation of planet parameters from the TESS data using a Monte-Carlo Markov Chain (MCMC) method, transit parameters bias caused by binning and a comparison between our values of inclination and R_p/R_* with previous estimates. Constraints on the exoplanet atmosphere and the predictions of R_p/R_* in the Kepler band and a z -band, which is sensitive to water vapor is presented in Section 3. In Section 4, we present a summary of our results.

2. DATA REDUCTION

2.1. TESS Photometry

The exposure time of TESS for each frame is 2 seconds. Due to data downlink limitations, two images products are released; the individual frames in a few pixels around certain sources are integrated to 2-minute cadence, and are called Target Pixel Files (TPF). The frames are also integrated to 30-minute cadence for all the sources in the field of view, to generate a Full Frame Image (FFI) (Ricker et al. 2015b). We use 2-minute cadence frames to derive the light curves and 30-minute cadence frames to calibrate and remove the blending flux from surrounding sources.

The FFI shows an offset in astrometry relative to the nominal position of the exoplanet host star, as measured by Gaia. However, the astrometric offset is similar across all the frames. So for each source, we checked the astrometry in a few frames and applied a few pixel-level offset if it is present. A smaller fractional offset is determined from a 2-dimensional Gaussian fit of the target. Example images after correcting for astrometric offsets are as shown in Figure 1. The numbers of frames for KELT-19Ab, WASP-156b, WASP-121b are 17612, 17612, and 15973, respectively. The median offsets for KELT-19Ab, WASP-156b, WASP-121b are 0.10, 0.27, 0.07 in pixels. The standard deviations are 0.04, 0.09, 0.04 in pixels.

The Target Pixel File (TPF) is a 11 pixels \times 11 pixels cutout of the image around the TESS Input Catalog (TIC). The pipeline versions are spoc-3.3.57-20190215 for KELT-

19Ab, spoc-3.3.51-20181221 for WASP-156b, spoc-3.3.57-20190215 for WASP-121b.

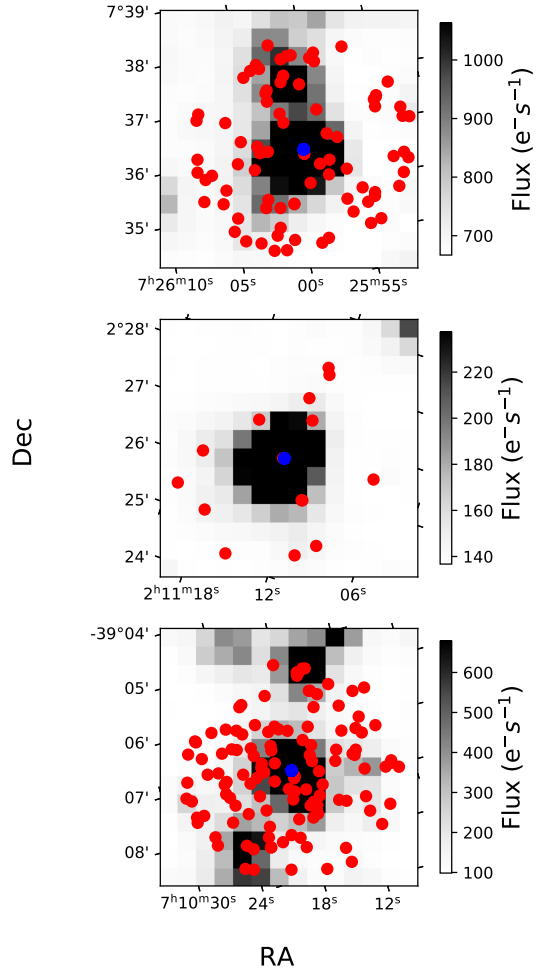


Figure 1. 14 \times 14 pixel TESS images of KELT-19Ab, WASP-156b, WASP-121b, from top to bottom, respectively. The blue markers indicate the position of the exoplanet host star in the Gaia catalog. The red markers indicate the position of nearby sources in the Gaia catalog which contaminate the photometry of the host star i.e. within 6 pixels separation. Each pixel in the image is 21''. The direction is North up, East to the left.

We measured the photometry of the host star in a circular aperture with TPF. The aperture radius was chosen to be 3 pixels, corresponding to 63''. The flux from pixels whose fractional area falls within the aperture is correctly accounted for. The sky background per image was estimated as the median of the pixels which constitute the lowest fifth percentile in flux and subtracted from the photometry in the aperture.

The standard deviation of these pixels yields the background noise in the photometry. The quadrature sum of this noise and the Poisson noise of the source itself is the photometric uncertainty of the data point. The contribution to the photometry from nearby unresolved stars was then removed based on the relationship between flux brightness profile and the distance to the Gaia centroid of the unresolved stars (details in the next section).

2.2. Correction for Blending Sources

We then corrected the photometry to remove the contamination from surrounding unresolved sources. We used external information from the Gaia database (Gaia Collaboration et al. 2016, 2018), including position, brightness in Gaia G and Rp bands. The Gaia Rp band is similar to the bandpass of TESS. However, it is less sensitive than the Gaia G band. For stars which have Rp band photometry from Gaia, we used its brightness information directly. For faint stars with no Gaia Rp band detection, we used their G band flux density and applied a median color correction which is the median flux density ratio between the Rp band and G band of stars in the vicinity.

In order to estimate the flux from these contaminating sources inside the aperture centered on the exoplanet host star, we used the TESS FFI data to derive the relationship between flux contamination and the distance between the center of the photometric aperture and a source. We chose 5 bright (brighter than 13 mag in Gaia G-band) and isolated sources from the TESS Input Catalog. It is difficult to guarantee complete isolation to within 6 TESS pixels but the bright stars were chosen to have no detectable companions in the image and the Gaia catalog showed an absence of sources within 5 mags of the bright stars. We divided the 6 pixel radius circle into a set of annuli, each of 0.25 pixel width. We then chose a set of positions that traverse the annulus circumference in 0.1 pixel steps. With each of these positions as center, we performed aperture photometry by measuring the flux density within a circular aperture of radius 3 pixels as for the exoplanet host star. Sky subtraction was performed as described in the previous section. The maximum separation between the center of the aperture and from the bright star position was allowed to be 6 pixels where the contamination is negligible. This is because TESS has a 90% ensquared energy within a half-width of 2 pixels.

Finally, we normalized the set of sky subtracted flux density measurements by the flux measured at zero separation. We repeated this for 5 targets and for each target we used 10 frames. The median and standard deviation of the normalized brightness profile for all these measurements is shown in Figure 2.

The relationship between distance and brightness profile was then estimated by the polynomial fitting of the data

pairs (see in Figure 2). We then apply this relation to every contaminating source whose brightness has been estimated as described above, to derive the flux density contributed by the blending source to the photometry of the exoplanet host star. This contaminating flux density, which is constant for a particular exoplanet host star, was then removed from our photometry values¹. The total contaminating flux percentage and uncertainty for the three stars is $6.22\% \pm 0.42\%$, $0.64\% \pm 0.03\%$ and $31.49\% \pm 1.79\%$ for KELT-19Ab, WASP-156b and WASP-121b respectively.

In addition, there is a possibility of blending from an unresolved binary companion. In the case of WASP-156b and WASP-121b, there is no evidence of a binary companion in past work (Delrez et al. 2016; Demangeon et al. 2018). In the case of KELT-19Ab, a nearby stellar companion was detected with the Palomar/Hale 200" telescope using the near-infrared adaptive optics (AO) system (Siverd et al. 2018). The stars have a measured magnitude difference of $\Delta J = 2.50 \pm 0.06$ and $\Delta K_s = 2.045 \pm 0.03$. The J band result is thought to be less reliable because of poor AO correction on the night of observations. So we used the magnitude difference in the K_s band as an estimate of the brightness of the companion star and its contamination to the TESS photometry, although we note that we have no constraint on the optical to near-infrared colors of the companion star.

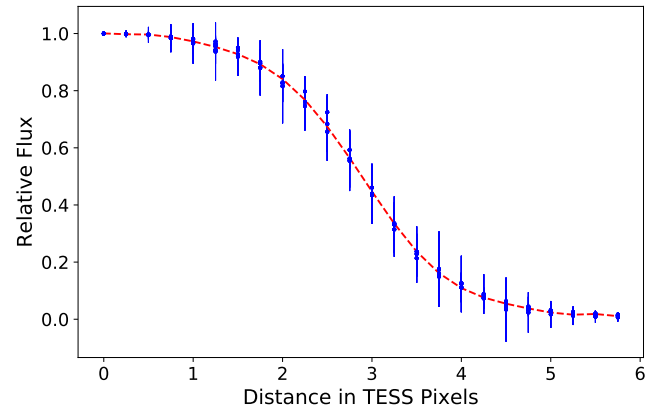


Figure 2. The normalized brightness profile of stars as seen by TESS used to estimate the amount of contamination of an exoplanet host stars' photometry by background stars seen by Gaia. The scatter points are the observed data. The red line indicates the polynomial fit to the data.

2.3. Detrending of the Light Curve

¹ The code to apply this correction is available at https://github.com/sailoryf/TESS_Deblending

Measuring an accurate transit depth of an exoplanet requires a high precision light curve. This requires detrending to remove the long term trends in the photometry outside of transit events (Gibson et al. 2012; Aigrain et al. 2015; Vanderburg & Johnson 2014; Smith et al. 2012). Since we already know the existence of an exoplanet around these stars, we can use prior knowledge of the transit mid-point time, period and transit duration to perform a simple detrending. To do this, we predicted the transit time in the TESS light curve and extract the parts of the light curve spanning 0.6 days centered at the transit mid-point.

The light curves during transit were then masked out, and we fitted a linear function to the masked cut-off light curve. The fit is used to estimate and remove the trending in the light curve within a day. We applied this correction for every single data point of the extracted light curve and fold the light curve around the transit midpoint to get the transit events shown in Figure 3. We also tried higher order polynomial function, including the order of 2, 3, 5 and 10. The difference between the detrended light curve is negligible for deriving the transit parameter.

2.4. Planet Parameters Derived from TESS-Detected Transits

2.4.1. Fitting with Free Inclination and Semi-major Axis

We used an MCMC fitting technique to derive the parameters of the exoplanets from the TESS transit curves (Mandel & Agol 2002). We adopted a circular orbit as in previous articles that confirmed the corresponding exoplanets with orbital periods derived therein (Siverd et al. 2018; Demangeon et al. 2018; Delrez et al. 2016). The value of T_{eff} , $\log g$, and $[Fe/H]$ was taken from the discovery articles as well. The free parameters in our fit are the radius ratio of the planet to the host star (R_p/R_*), the inclination of the planets orbit (i), the semi-major axis in unit of stellar radii (a/R_*), time offset of transit center (T_0) and the limb darkening parameters (a_1 for linear limb-darkening coefficient, a_2 for quadratic limb-darkening coefficient), as shown in table 1. Except for limb darkening, the other parameters have uniform priors.

We adopted the common inclination prior of $\mathcal{U}[70,90]$ but changed it to be $\mathcal{U}[70,110]$ when the posterior of inclination is within a degree of 90 degrees. This is because the distribution of inclination performs differently when the real inclination is close to 90. A prior cut-off at 90 degree severely distorts the posterior distribution to be non-Gaussian. A prior with no 90-degree cut-off yields a more reasonable posterior distribution. The difference in inclination posterior between these two scenarios of priors is systematic, but consistent within 1σ .

The limb darkening model is the same as that adopted in the exoplanet discovery articles (Siverd et al. 2018; Demangeon et al. 2018; Evans et al. 2017). The coefficients for limb

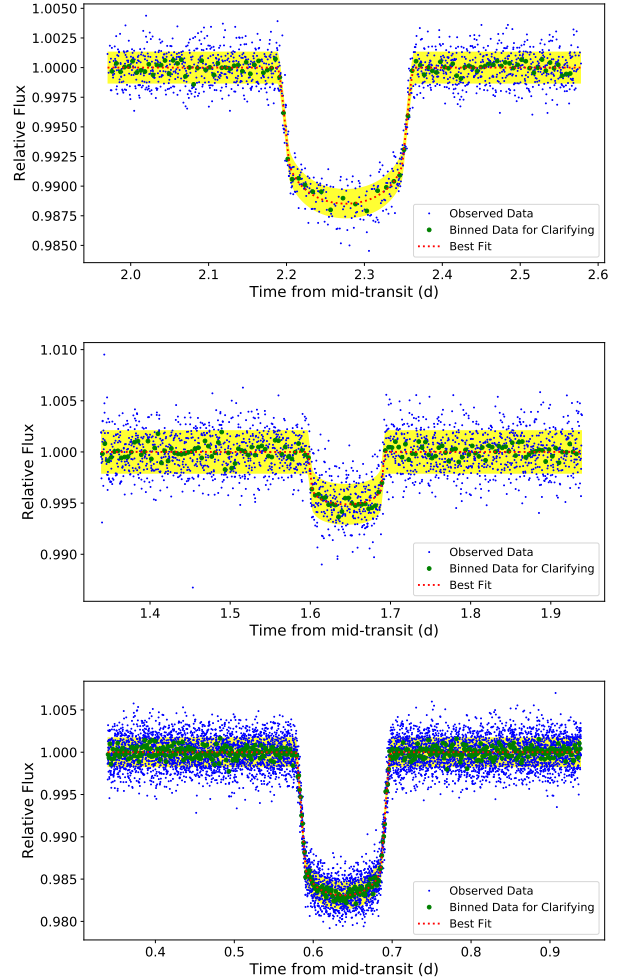


Figure 3. Fits to the TESS TPF transit light curves of KELT-19Ab (top), WASP-156b (middle), WASP-121b (bottom). The blue points are observed 2 minute data decontaminated using Gaia photometry. The green points are bins of 30 minutes cadence data. The red dashed line represents the best-fit transit model to the 2 minute data. The yellow region shows 1σ confidence region of the fits. The midpoint of the transit event is shifted to half the period, at the center of the x-axis. The free parameters in the fits are inclination, semi-major axis and limb darkening parameters as shown in Figure 4.

darkening have a Gaussian prior centered on the prediction for TESS data (Claret 2018) with an uncertainty of 0.05.

In the case of KELT-19Ab, we adopted T_{eff} , $\log g$, and $[Fe/H]$ of 7500 ± 110 K, 4.127 ± 0.029 cgs, -0.12 ± 0.51 . As in Siverd et al. (2018), a quadratic limb darkening model is applied. The priors for the limb darkening coefficient are 0.27 ± 0.05 , 0.23 ± 0.05 , for the linear (linLimb) and quadratic coefficients (quadLimb), respectively.

In the case of WASP-156b, the T_{eff} , $\log g$, and $[Fe/H]$ values are 5871 ± 57 K, 4.35 ± 0.03 cgs, 0.10 ± 0.10 . A quadratic limb darkening model is used (Demangeon et al. 2018).

The priors for limb darkening coefficients are 0.36 ± 0.05 and 0.22 ± 0.05 for linLimb and quadLimb respectively.

In the case of WASP-121b, the T_{eff} , $\log g$, and [Fe/H] values are 6460 ± 140 K, 4.2 ± 0.2 cgs, 0.13 ± 0.09 . The limb darkening model used is the quadratic limb darkening model (Delrez et al. 2016; Evans et al. 2018). The limb darkening coefficients that we applied to our MCMC fits are 0.33 ± 0.05 , 0.21 ± 0.05 , respectively.

For each fitting, the parameters' probability distributions are derived using Python MCMC tool, PYMC (Patil et al. 2010). We applied 200000 iterations for the whole chain, and ignore the first 100000 steps to ensure the chain is stable. The best-fitting light curves are shown in Figure 3, respectively. The distribution of R_p/R_* , a/R_* , inclination and limb darkening parameters are shown in Figure 4. The best fit results are shown in Table 1.

The inclinations derived from TESS TPF data for KELT-19Ab, WASP-156b, and WASP-121b are 3.5, 1.0 and 2.3 degrees larger than the results based on identification paper, respectively. Specifically, in case of WASP-121b, the inclination derived is more consistent with the follow-up work value 89.1 by Evans et al. (2018). Due to TESS's continuous sampling with 2 minutes and high precision photometry, the ingress and egress of transit are well monitored. These short phases in the transit duration are extremely sensitive to the inclination and semi-major axis. We, therefore, believe that the TESS result as well as result from Evans et al. (2018) on inclination for WASP-121b are robust.

2.4.2. Fitting with Fixed Inclination and Semi-major Axis

Although our best fits are similar to other work, there are clear signs of differences, particularly in our derived inclination and transit depths. In order to focus on differences in the radius ratio caused by wavelength dependent properties, we refit the TESS light curves, by fixing the inclination and semi-major axis to the referenced work (Siverd et al. 2018; Demangeon et al. 2018; Evans et al. 2017).

The fitting followed the same procedure as section 2.4.1. The fitting results, as well as the derived parameters from previous work, are listed in Table 1. The differences between our fits and the result from the former work are shown in Figure 5. The reduced chi-square in the fits are slightly larger than the best fit from previous section (Table 1). The small difference in the chi-square values indicate that the value of inclination and semi-major axis preferred in other work, is reasonably consistent with the TESS data but is not the preferred solution.

The fixed parameter MCMC fits have reduced uncertainties due to the strong priors on inclination and semi-major axis. These constraints on inclination and semi-major axis disturb the Gaussian distribution of other parameters. The revision for the three sigma rules for the parameters is beyond

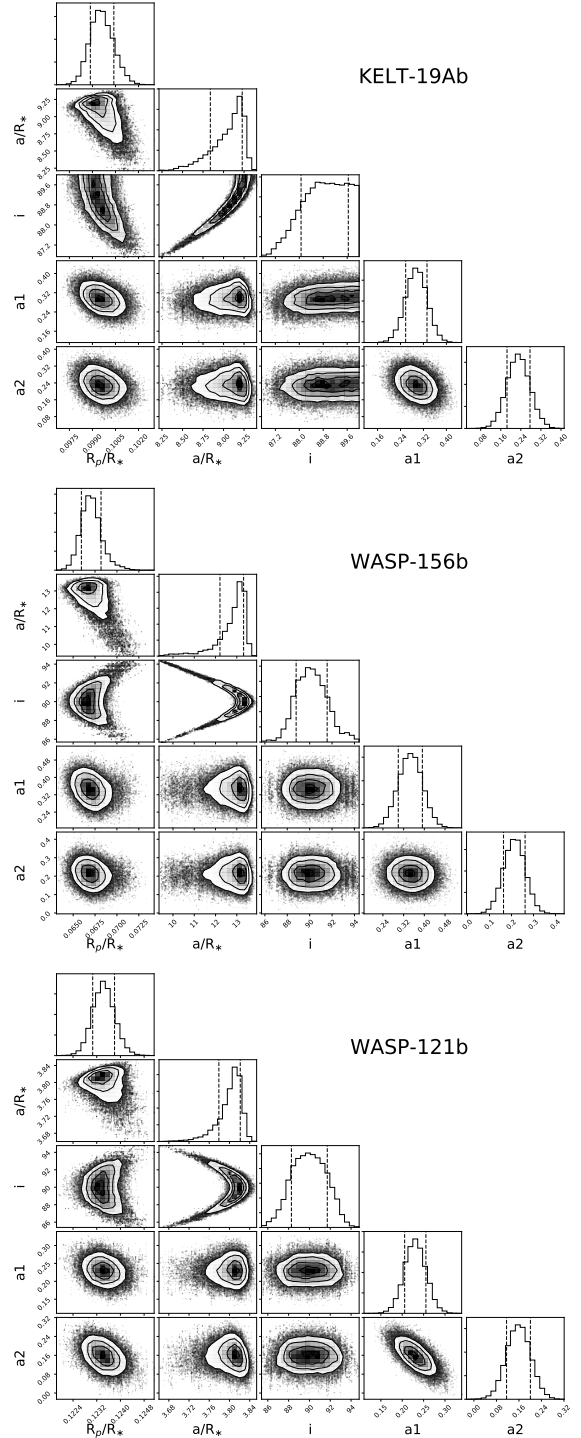


Figure 4. The probability distribution of the fit parameters for KELT-19Ab (top), WASP-156b (middle), WASP-121b (bottom). The grayscale map indicate the density of samples derived from MCMC analysis for different pairs of parameters. The histograms along the diagonal are the marginalized density distribution for individual parameters. The dashed lines denote 68% of samples.

this work (see in reference Pukelsheim 1994; MacKay 2002;

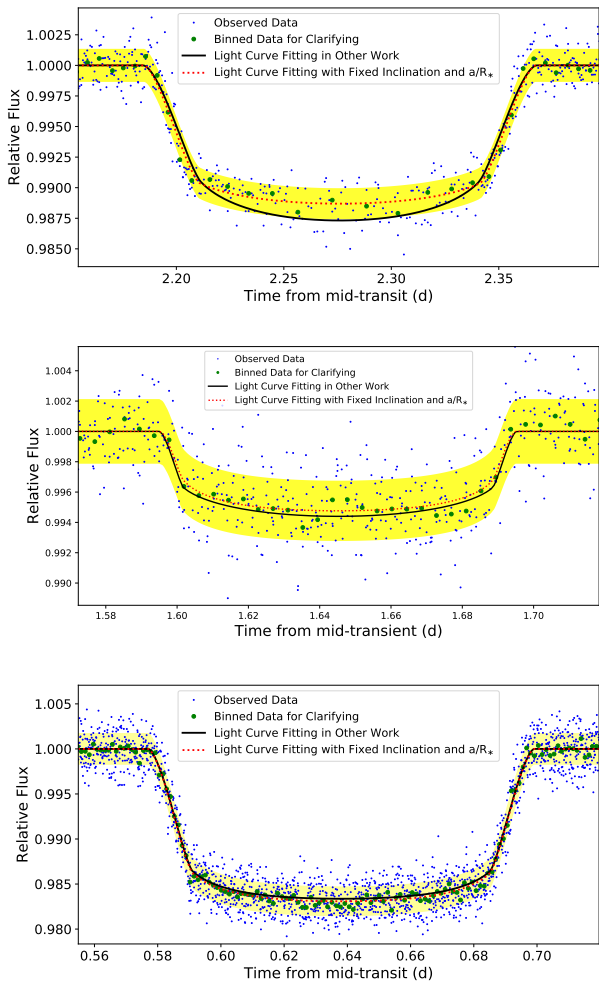


Figure 5. Results from fitting with fixed inclination and semi-major axis for KELT-19Ab (top), WASP-156b (middle), WASP-121b (bottom). The blue points are deconfused photometry. The green points indicate 30 minutes cadence binned result. The red dashed line represents best-fitting model. The black line indicates the result of previous work (referenced in the text). The yellow region shows 1σ confidence region of the fitting. The transit event is shifted at the center of x-axis which is half of the period.

Hogg & Foreman-Mackey 2018). We cited the 1σ uncertainty from the MCMC derived standard deviation for each parameter.

Our fits to the TESS data gives us a consistent planet to star radius ratio for WASP-121b and WASP-156b at the $\sim 2\sigma$ level (Table 1). However, the planet to star radius ratio for KELT-19Ab is 3.5σ smaller than previous work (Siverd et al. 2018). The TESS radius ratio for WASP-121b is deeper than the median value including all the bands with the TESS wavelength range from (Evans et al. 2018). For WASP-156b, the radius ratio is smaller than past work (Demangeon et al. 2018)

2.5. Transit Parameters Bias Caused by Binning

Sampling cadence results in morphological distortions to the transit light curve due to sampling of transit ingress and egress (Kipping 2010). For the TESS cadence, an assessment of the parameter bias is necessary for assessing the differences in transit depths for different bands.

We firstly investigate if our derived parameters from the TESS 2 minute data are consistent with that from the 30 minute data by repeating the whole data reduction and fitting with 30 minute cadence image. In case of free inclination fitting, the inclinations derived for KELT-19Ab, WASP-156b, and WASP-121b are 4.8, 5.1 and 13.6 degrees smaller than the results based on 2 minutes binning data, respectively. Furthermore, the residuals from the light curve for WASP-121b when fixing the inclination shows obvious structure during the phase of ingress and egress (seen in Figure 6). The radius ratio when fixed inclination and semi-major axis is 0.1195 ± 0.0004 , about 7σ smaller than 2 minutes result, with substantially worse chi-square values. The inconsistency, especially for WASP-121b, motivates a simulation for a more detailed assessment of the differences.

We simulated 1000 light curves for each source. The input parameters were set to that in the discovery papers (Table 1 Siverd et al. 2018; Demangeon et al. 2018; Delrez et al. 2016). We note that for WASP-121b, the newest reported inclination is 1.5 degrees larger than initially assessed (Evans et al. 2018). The result from Evans et al. (2018) is also well matched to the TESS TPF derived result as shown in Table 1. But for the purpose of the simulations, we chose the value from the discovery paper. The time sampling for the simulated light curve is 1 second and is binned to 2 minutes and 30 minutes. The numbers of transit events are set to be the same as the event numbers observed by TESS. We add a Gaussian error to the light curves. The adopted 1σ scatter is the standard deviation of the residuals from fitting the TESS light curves scaled by a factor of the square root of time scale.

These simulated light curves are then fit as described earlier. Figure 7 and 8 show the distribution of derived parameters compared to the input values. We find that the magnitude of bias in the derived parameters especially inclination and semi-major axis, depends on the duration time of the transit, especially ingress and egress. We take WASP-121b as an illustrative example which gives the largest inclination difference. The derived median inclination value with the 30 minute cadence data is 76.4deg with a standard deviation of 0.7, 11.2 degrees smaller than the input value. The inclination decrease is because the binning smooths the rapid change of the flux decrease during ingress and egress. The planet to star radius ratio when fixing the inclination and semi-major axis is 0.1201 ± 0.00035 , also smaller than the input value at the level of $\sim 5\sigma$ (seen in Figure 7).

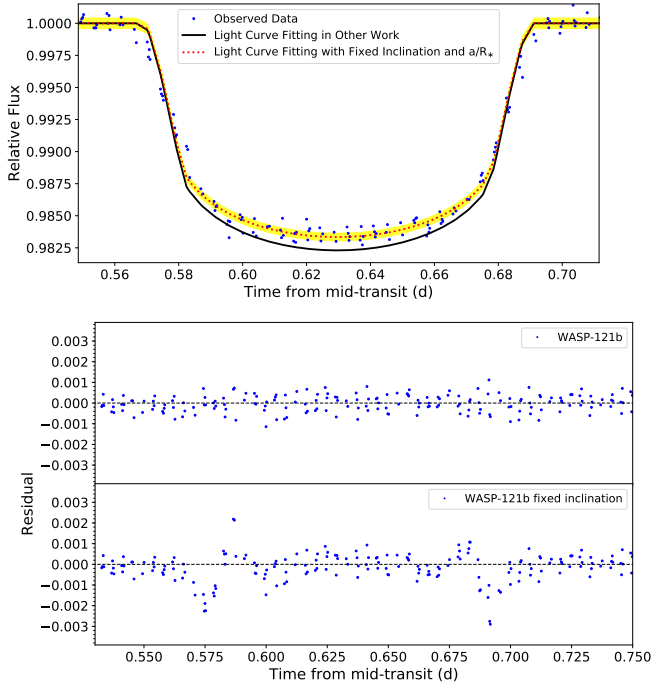


Figure 6. Top: Result from fitting with a fixed inclination and semi-major axis for WASP-121b (TESS 30 minute data). The red dashed line represents the best-fitting model. The black line indicates the fit from previous work. Bottom: Residuals after fitting for the exoplanet transit around transit midpoint for WASP-121b based on 30 minutes data. The upper panel is residuals from the best fit. The lower panel is residuals assuming a fixed inclination and semi-major axis adopted from previous work. The 30 minutes data are clearly inconsistent with the previously derived inclination value.

In the case of light curves with 2 minute sampling, the bias is assessed in the same way. The best fit inclination for WASP-121b is found to be 87.7 ± 1.3 deg. The planet to star radius ratio with a fixed inclination and semi-major axis is 0.1219 ± 0.0004 . We find the difference between the derived values and the input values to be negligible with the 2 minute data.

For all three sources, we find that the simulations with 2 minute sampling yield similar parameters as the input value. Meanwhile, with 30 minutes cadence, the result is significantly biased. Also, the differences in the inclination and planet-to-star radius ratio between 2 and 30 minutes cadence matches the difference between them from real TESS data. From these simulation, we therefore conclude that the biases in parameters from fitting TESS data of different cadence comes from binning, and that the fit parameters from the 2 minute cadence data for our three targets are robust.

Finally, we undertake a simulation to investigate the dependence of inclination and semi-major axis upon sampling time interval (Figure 8). The sampling time interval in the

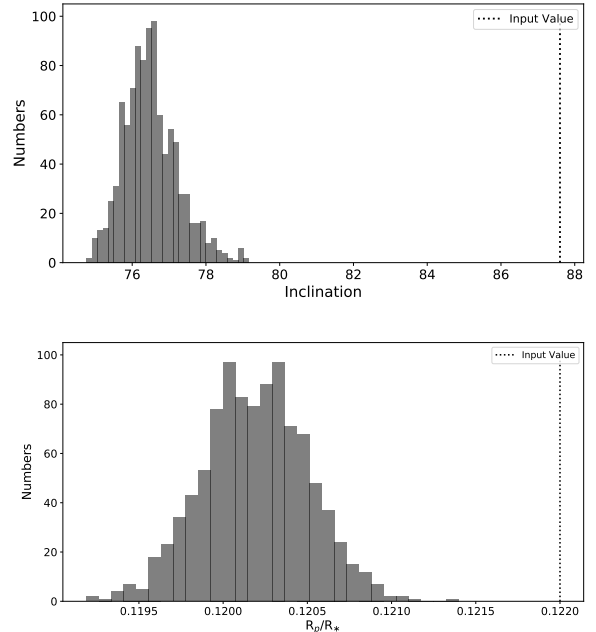


Figure 7. Top: The derived inclination distribution from fitting 1000 simulated light curves sampled at 30 minutes, for the parameters of WASP-121b. Bottom: The planet to star radius ratio distribution when fixing the inclination and semi-major axis. The vertical line for both panels gives the input value to the simulations. Clearly, for WASP-121b, a light curve cadence of 30 minutes would result in a large bias in derived parameters.

simulation ranges from 1 minute to 50 minutes. For each interval, the light curve is generated as described above and fit. We duplicate 10 simulations for each sampling interval. The median fit values and standard deviations of the derived parameters are shown in Figure 8 for each sampling interval. It is clear that the inclination and semi-major axis are not significantly biased when the sampling time is less than 5 minutes. Also, the result indicates that the inclination and semi-major axis derived are distorted to be smaller when applying a larger sampling interval (as shown in Figure 8). This suggests that great care must be taken when comparing transit depths in different bands, especially when the light curve sampling intervals are likely to be quite different.

2.6. A difference in stellar activity level?

As explained in Pont et al. (2008); Agol et al. (2010), differences in the number of starspots between past observations and the TESS observations could account for differences in the measured transit depth. It was estimated that when the flux density of the star changes by 1% because of stellar spots, the influence on the radius ratio is of the order of $10^{-3} R_p/R_*$, comparable to the uncertainty of our TESS derived value. None of the three sources studied in this paper (Siverd et al. 2018; Demangeon et al. 2018; Evans et al.

Table 1. Planet Parameters

Parameters	Description	KELT-19Ab 68% Confidence	WASP-156b 68% Confidence	WASP-121b 68% Confidence
Best Fitting Parameters				
R_p/R_*	Planet/star radius ratio in TESS	0.09955 ± 0.00074	0.0670 ± 0.0012	0.1234 ± 0.0004
i [deg]	Inclination	88.9 ± 0.7	90.1 ± 1.4	89.9 ± 1.6
a/R_*	Semi-major axis of planet orbit in unit of stellar radii	9.10 ± 0.19	12.98 ± 0.73	3.81 ± 0.03
std of residual	Parts per million	1357	2130	1763
reduced χ^2	Reduced chi-square	1.0008	1.0009	1.0004
Fitting Results with Fixed Inclination and Semi-major Axis				
R_p/R_*	Planet/star radius ratio in TESS	0.10349 ± 0.000048	0.0662 ± 0.0009	0.1230 ± 0.00025
	Planet/star radius ratio in other work	0.10713 ± 0.00092^a	$0.0685^{+0.0012e}_{-0.0008}$	$0.1220^{+0.0005}_{-0.0005} b,c,d$
difference significance	Difference between TESS and former work in σ	3.508	1.533	1.789
i [deg]	Inclination	$85.41^{+0.34a}_{-0.31}$	$89.1^{+0.6d}_{-0.9}$	$87.6 \pm 0.6^{b,c}$ 89.1 ± 0.5^d
a/R_*	Semi-major axis of planet orbit in unit of stellar radii	$7.50^{+0.20a}_{-0.18}$	$12.8^{+0.3e}_{-0.7}$	$3.754^{+0.023}_{-0.028} b,c$ 3.86 ± 0.02^d
std of residual	Parts per million	1375	2132	1765
reduced χ^2	Reduced chi-square	1.020	1.001	1.002
linLimb	Linear limb-darkening coefficient	0.29 ± 0.04	0.37 ± 0.04	0.24 ± 0.03
quadLimb	Quadratic limb-darkening coefficient	0.23 ± 0.04	0.23 ± 0.04	0.21 ± 0.04

Reference:

- (a) Siverd et al. (2018);
- (b) Delrez et al. (2016);
- (c) Evans et al. (2017);
- (d) Evans et al. (2018);
- (e) Demangeon et al. (2018);

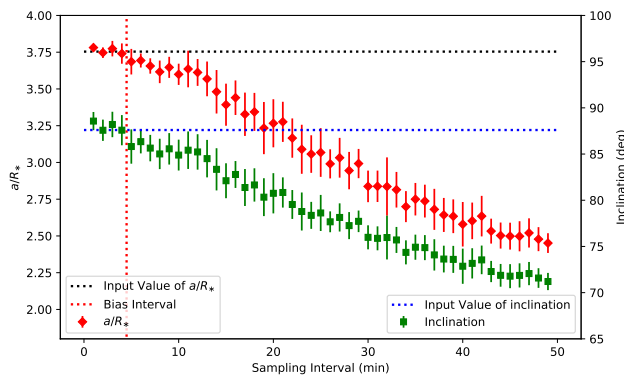


Figure 8. Results from fitting inclination (green squares) and semi-major axis (red diamonds) to simulated light curves of different sampling intervals. The vertical red dotted line gives the sampling interval limit below which the parameters derived are not biased and corresponds to 5 minutes. The horizontal black line dotted is the input value of the semi-major axis; the dotted blue line is the input value of inclination. Clearly, TESS FFI 30 minute cadence data would result in significantly biased parameters for planets with short duration transits such as those considered here.

2017) have shown any past evidence of stellar activity. Furthermore, if starspots were significant, the standard deviation of the light curve outside the transit should be different from that during transit. So we conclude that the impact of starspots on our transit depth measurement is negligible.

3. ATMOSPHERIC CONSTRAINTS

Our primary scientific motivation for undertaking this work was to compare R_p/R_* in the TESS band with the value from previous work to constrain the atmospheres of the exoplanets. In particular, the TESS bandpass is significantly redder than the *Kepler* band and encompasses the $0.95 \mu\text{m}$ water feature. The presence of these features in the planets' atmosphere would result in a larger value of R_p/R_* in the TESS band. For instance, the R_p/R_* of KELT-19Ab in TESS data is significantly smaller, at the level of 3.5σ , indicating the existence of atmospheric features.

Our fixed inclination fits (Table 1) allow for a more direct comparison with past work. The significance level of differences in R_p/R_* are 3.5 , 1.5 , 1.8σ for KELT-19Ab, WASP-156b and WASP-121b, respectively. We discuss the implications of this difference for each of the exoplanets.

3.1. KELT-19Ab

KELT-19Ab is a giant planet transiting a moderately bright ($V \sim 9.9$ mag) A8V star with a orbital period of 4.61 days (Siverd et al. 2018). The host stars has $M_* = 1.62^{+0.25}_{-0.20} M_\odot$, $R_* = 1.83 \pm 0.10 R_\odot$. The planet has a radius of $R_p = 1.91 \pm 0.11 R_J$.

KELT-19Ab has R_p/R_* of 0.10713 derived from a joint fit to ground-based (U, B, V, R, I, Sloan g', r', i', z') data. In order to derive an atmospheric constraint, we need to derive the value of R_p/R_* in each band. We treated the joint value of R_p/R_* as the value in each band. The uncertainty follows the equation: $\sigma_{joint} = \sigma_i / \sqrt{N}$, according to the error propagation law. σ_{joint} is the joint band uncertainty, N is the number of bandpasses, σ_i is the uncertainty in the band i . Since we do not have access to the ground-based data, we assume the uncertainty in each band is the same. We compared these values with TESS derived fixed-inclination R_p/R_* in Figure 9.

We fitted the data with the grid of atmospheric transmission spectra from Goyal et al. (2019, 2018) which are developed for hot, H₂/He dominated Jupiters. This model is a 1D radiative-convective-equilibrium solution based on the ATMO code (Tremblin et al. 2015, 2016; Drummond et al. 2016). ATMO solves the radiative transfer for isothermal pressure-temperature (P-T) profiles, with opacity and chemical abundance being other parameters. The grid model has a parameter space of two chemical scenarios, 22 temperatures, 4 planetary gravities, 5 atmospheric metallicities, 4 C/O ratios, 4 scattering haze, 4 cloud parameters and a scaling factor to the specific planetary radius. Modifying specific chemical abundance will lead to different chemical equilibrium which is avoided in the use of the forward grid model.

In order to fit the model, we minimized the chi-square value between the observations and model predictions at all the bands. The model prediction at each band is derived by the following equation where S_λ is the filter response.

$$\frac{R_p}{R_*} = \frac{\int \frac{R_p}{R_*} S_\lambda d\lambda}{\int S_\lambda d\lambda} \quad (1)$$

We found that the haze dominated model at 1500K is the best fit with $\chi^2 = 5.13$. A clear model showing strong water vapor with rainout condensation at 1000K is the second best fit with $\chi^2 = 6.2$, while a clear model showing weak water vapor with rainout condensation at 1500K is the third best fit with $\chi^2 = 6.5$. A flat model with opaque featureless is also shown with an of $\chi^2 = 7.1$ which is not a good explanation so far. Other models had much larger chi-square values (more than 10) and are not consistent with the data. The significant smaller value of χ^2 from haze model yields a probable atmosphere feature for present data.

We predicted the possible R_p/R_* value in the *Kepler* band and $z-$ band based on these templates (Figure 9). The difference between R_p/R_* in the *Kepler* band relative to the TESS band is most effective for characterizing the strength of haze. The *Kepler* band would yield 0.1047 for haze dominated atmosphere and 0.1042 for a clear model. The presence of water would cause a significant difference in the $z-$ band prediction. The prediction of R_p/R_* is 0.1047 from clear model with strong water contribution. The value is 0.1035 from a clear model with faint water, as well as from a haze dominant model.

We find that a difference of 1.1% in R_p/R_* arises between strong water contribution and faint water contribution models. This implies that with 500ppm precision for 200 data points around transit event in the $z-$ band, one can distinguish between these two scenarios. The prediction for precision and data amount is based on the light curve fitting from this work. The requirement precision depends on the square root of the number of data points.

3.2. WASP-156b

The discovery of WASP-156b was reported in Demangeon et al. (2018). It is a super-Neptune orbiting a K type star ($V=11.6$ mag, $M_* = 0.842 \pm 0.052 M_\odot$, $R_* = 0.76 \pm 0.03 R_\odot$) with a period of 3.84 days. It has a mass of $0.128^{+0.010}_{-0.009} M_J$, a radius of $0.51^{+0.02}_{-0.02} R_J$.

We followed the same procedure as for KELT-19Ab, to analyze the differences in R_p/R_* in different bands. The value of R_p/R_* is taken from Demangeon et al. (2018) at Johnson R, Gunn r, Johnson I and Gunn z (Figure 10).

A clear atmosphere at 1500K with strong water contribution (best fit model) has a χ^2 of 2.35 while the faint water model and the haze dominant model at the same temperature follows with a worse χ^2 of ~ 2.44 . A model with an opaque featureless model is as good as the best fit model with a χ^2 of 2.35. The strong water contribution causes a shift of 0.9% in $z-$ band prediction of R_p/R_* compared to the faint water model. In the Kepler band, the haze dominant model has a larger R_p/R_* of 1.3% than the no atmosphere model. We conclude that the current measurements are consistent with an opaque featureless model.

3.3. WASP-121b

WASP-121b was discovered by Delrez et al. (2016). It is a hot Jupiter around a main sequence star ($V=10.4$ mag, $1.353^{+0.080}_{-0.079} M_\odot$, $1.458 \pm 0.030 R_\odot$) with a period of 1.28 days. The planets has a mass of $1.183^{+0.064}_{-0.062} M_J$ and a radius of $1.865 \pm 0.044 R_J$.

We used external observations from Delrez et al. (2016); Evans et al. (2016, 2018) in conjunction with our analysis of the TESS data (Figure 11). These measurements utilized the standard ground-based filter, STIS, and WFC3 instruments

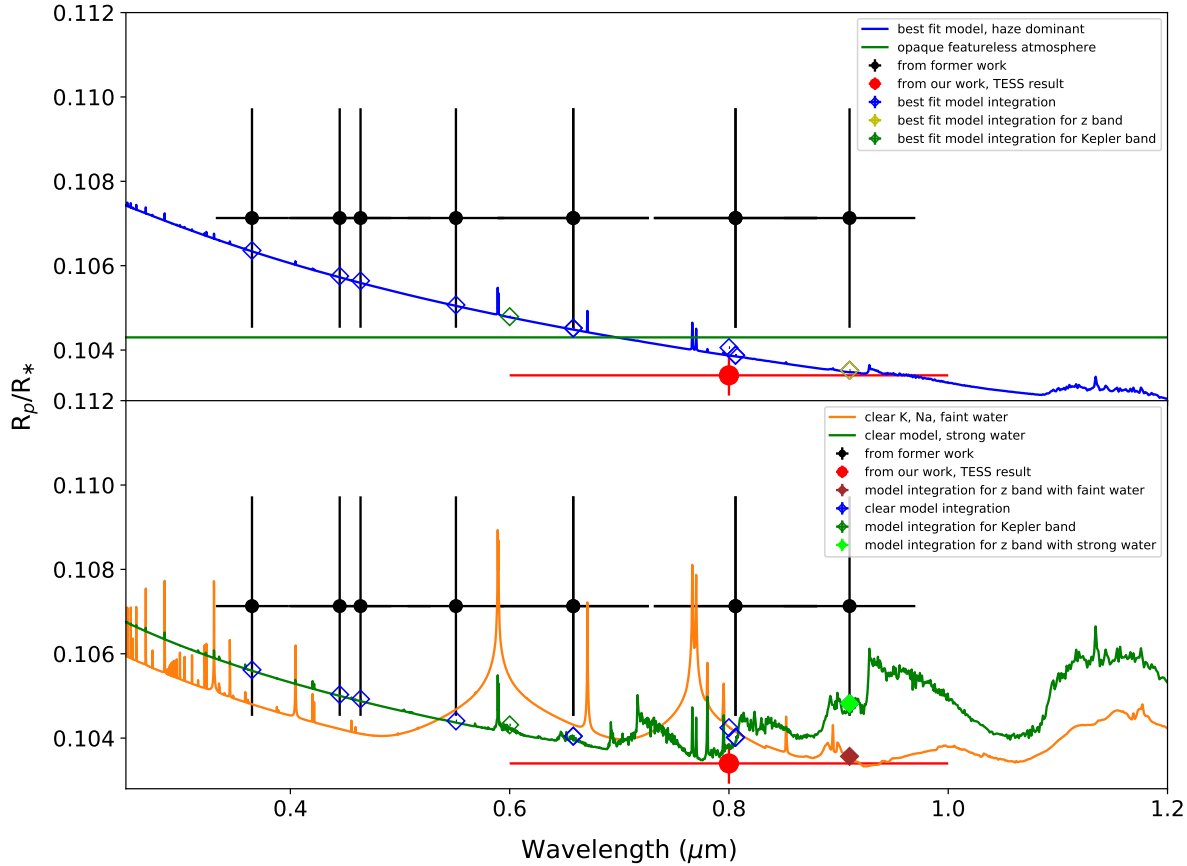


Figure 9. R_p/R_* of KELT-19Ab in different bandpasses. The red point is R_p/R_* derived from TESS. The black points are R_p/R_* from former work. In the top panel, the best fit model (haze dominant) is shown as a blue solid line. The green line indicates a flat, opaque featureless model that is consistent with the data. Blue diamonds are best-fit model predictions at the bands. The yellow diamond is the best fit model prediction at the SDSS z band, green diamond is the best-fit model prediction at the Kepler band. In the bottom panel, a clear model with strong water (green) is shown with a faint water model (orange) as a comparison. Blue diamonds are strong water model predictions in different wavelengths bands while the green diamond is for the *Kepler* band. Dark green and brown diamonds are the strong water and faint water model prediction in the SDSS z -band. Clearly, 500ppm photometry in the z -band can distinguish between these scenarios.

on *Hubble* and span 0.3 to $1.65\mu\text{m}$. As outlined in Evans et al. (2018), a global fit for the whole spectrum is challenging due to the complex problem of non-equilibrium chemistry.

Our fits with the inclination fixed to past work however, yield a value of R_p/R_* which is in very good agreement with Evans et al. (2018). The median value of the radius ratio is 0.1225 at the wavelength arrange of TESS. To fit the spectrum, we again use the general grid model from Goyal et al. (2019).

The best-fit model from Evans et al. (2018) is still the best fit model when we add the TESS constraints. The fitting has a reduced chi-square of 5.138, with 92 data points and 8 fitted parameters. The model is with local condensation, temperature of 1500K, gravity at 10ms^{-2} , atmospheric metallicities at 20x, C/O ratio of 0.7, haze parameters of 1.0 and no cloud (in

Figure 11). Meanwhile, an opaque featureless model is also consistent with the data (reduced chi-square is 5.629). The haze dominant model is with a chi-square of 6.360. A transmission model at 1500K with a clear existence of potassium, sodium and water vapor has a much larger reduced chi-square of 28.707 and seems to be ruled out. We conclude therefore that the TESS measurements are consistent with both Evans et al. (2018) best fit model and the haze model.

4. SUMMARY AND DISCUSSION

We have analyzed the TESS data for KELT-19Ab, WASP-156b, WASP-121b to measure R_p/R_* in a broadband spanning 600nm to 1000nm. We identify the significant role of contamination by unresolved background stars in the TESS data and use Gaia data to subtract their contribution to the

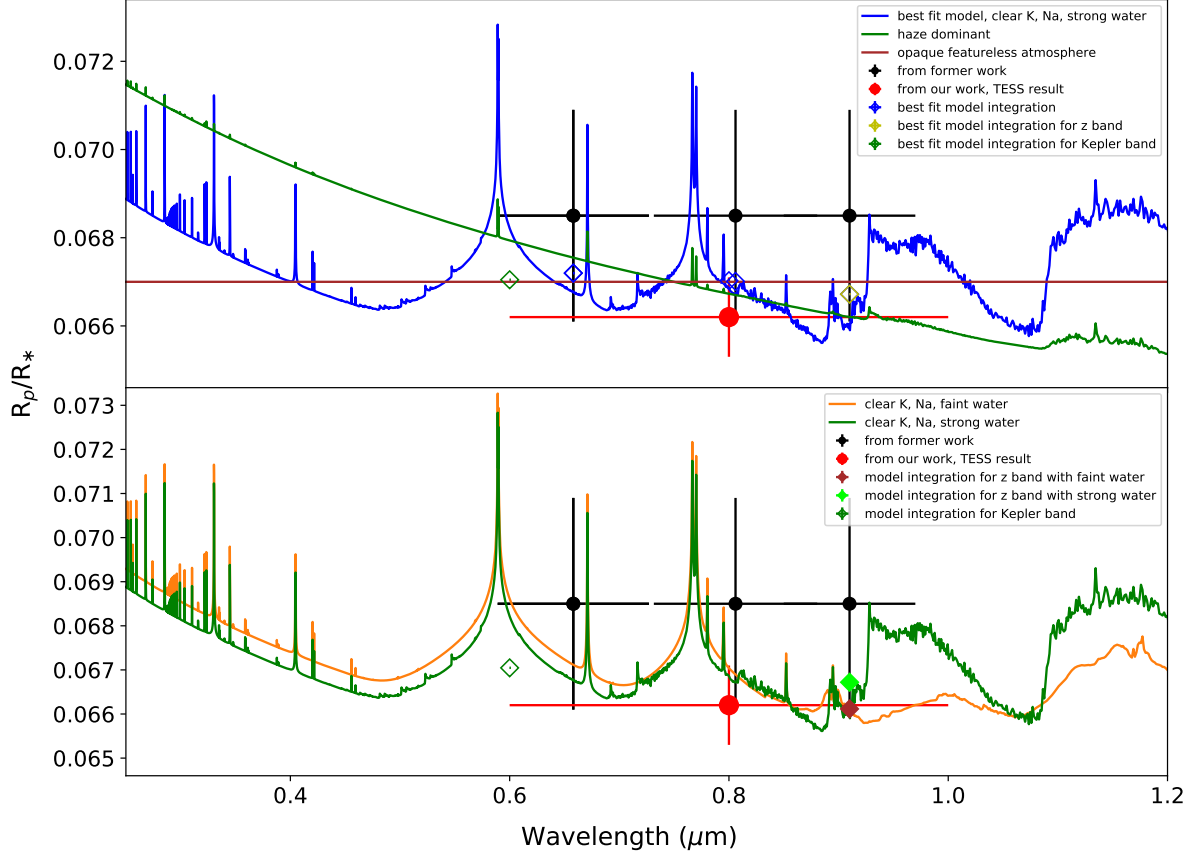


Figure 10. R_p/R_* of WASP-156b in different bandpasses. The top panel shows the clear model with strong water (blue solid line), the haze dominant model (green solid line) and the opaque featureless model (brown solid line). The red point is R_p/R_* derived from TESS. The black points are R_p/R_* from former work with the blue diamonds the "clear model" predictions at those bands. The yellow diamond is the model prediction at the SDSS z -band, green diamond is the model prediction at Kepler band. In the bottom panel, a clear model with strong water (green solid line) is shown along with a faint water model (Orange solid line) for comparison. The empty green diamond is a strong water model prediction at the Kepler band. The dark green diamond is the strong water model prediction at the SDSS z -band. Brown diamond is faint water model prediction at z -band.

transit light curves. We provide general-purpose software to address this issue for all TESS data. We detrend the light curves through a linear fit to the photometry near the transit events. To derive the exoplanet transit parameters, we performed two ways of MCMC model fitting: with and without inclination and semi-major axis fixed. The former in particular helps with the comparison with past work on these stars. Using simulations, we estimate the systematic bias for inclination and radius ratio with 30 minutes cadence data. We find the inclination and semi-major axis are distorted to be smaller when we apply a larger sampling time interval. However, we find that 2 minute sampling does not cause any bias for transit parameters. The atmosphere of these three exoplanets was then constrained based on R_p/R_* in different bands.

In the case of KELT-19Ab, we find that the TESS-measured R_p/R_* is $\sim 3.5\sigma$ smaller than past work. The model fitting favors a haze dominant atmosphere. In the case of WASP-156b, we find that the TESS transit depths agree with previous work and prefer a no atmosphere model fit to the measurements. In the case of WASP-121b, the fits to the TESS light curve prefer the newest reported inclination. We find that the atmospheric transmission spectrum is best fitted with a 1500K model with water vapor as reported before. However, a no atmosphere model is just as consistent with the data, somewhat weakening the evidence for water vapor in this exoplanet atmosphere.

Our work shows that exoplanet atmospheric model constraints benefit from high precision continuous photometry which provides strong constraints on key parameters such as

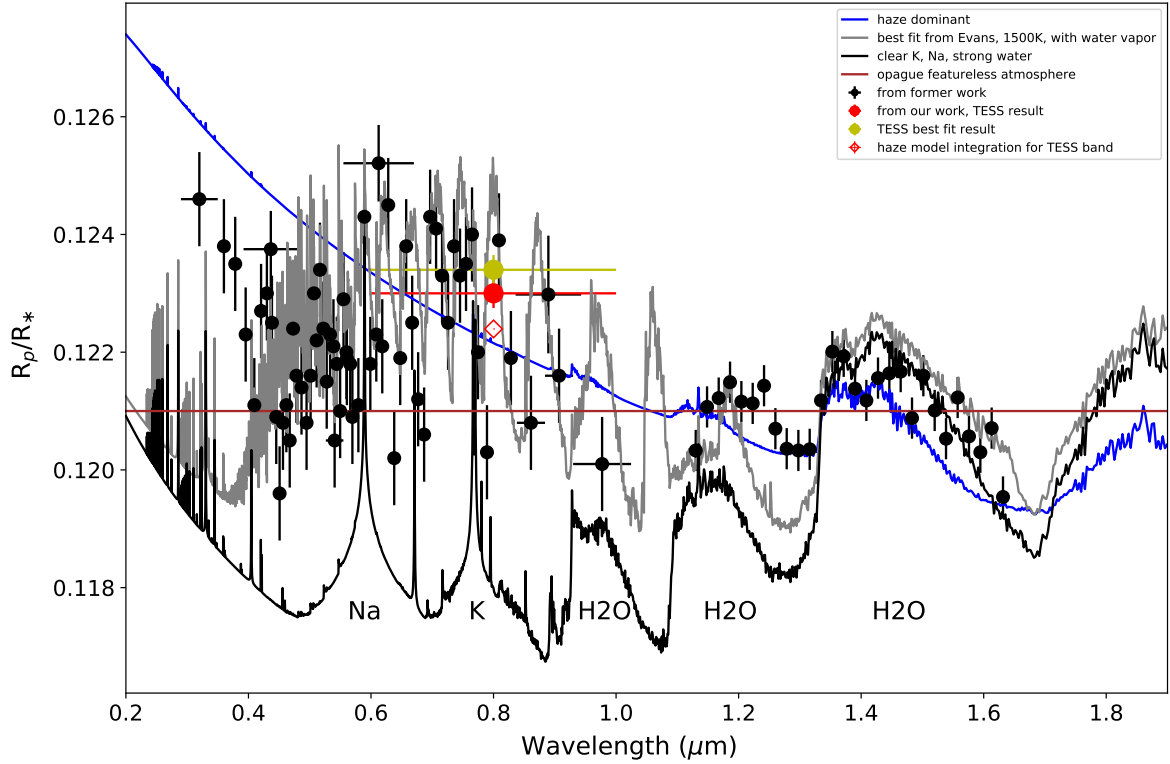


Figure 11. The transmission spectrum for WASP-121b. The solid yellow point is the best fit value of R_p/R_* from the TESS light curve. However, if the inclination is fixed to previous work for a consistent comparison, the solid red point is R_p/R_* derived from TESS data. The black points are R_p/R_* from former measurements. The grey solid line is the best fit from Evans et al. (2018). The blue line shows the haze model. The brown line shows the opaque featureless model. The black line indicates a clear atmosphere at a cool temperature (shifted for clarity).

inclination. Adding one high precision observation at certain bands improves the constraints on atmospheric composition. In a few months, when TESS observes the Northern Hemisphere, we will have Kepler (Borucki et al. 2010) and TESS constraints on a few bright stars, which will help assess the role of haze in exoplanet atmospheres. Finally, we show that precision photometry with \sim 500ppm to 1000ppm in the z -band can help directly constrain the presence of water vapor in the exoplanet atmosphere, when combined with precise TESS photometry.

We are very grateful to the thoughtful comments by a referee which greatly improved the quality of results presented in this manuscript. This work made use of PyAstronomy² and the NASA Exoplanet Archive. We would like to thank Jayesh M. Goyal for useful inputs and discussion and Caltech Optical Observatories for supporting the visit by the lead author. We also thank Hilke Schlichting for useful feedback

on the manuscript. Fan Yang and Ji-Feng Liu acknowledge funding from National Natural Science Foundation of China (NSFC.11988101), National Key Research and Development Program of China (No.2016YFA0400800) and National Science Fund for Distinguished Young Scholars (No.11425313).

² <https://github.com/sczesla/PyAstronomy>

REFERENCES

- Agol, E., Cowan, N. B., Knutson, H. A., et al. 2010, *ApJ*, 721, 1861, doi: [10.1088/0004-637X/721/2/1861](https://doi.org/10.1088/0004-637X/721/2/1861)
- Aigrain, S., Hodgkin, S. T., Irwin, M. J., Lewis, J. R., & Roberts, S. J. 2015, *MNRAS*, 447, 2880, doi: [10.1093/mnras/stu2638](https://doi.org/10.1093/mnras/stu2638)
- Berta, Z. K., Charbonneau, D., Désert, J.-M., et al. 2012, *ApJ*, 747, 35, doi: [10.1088/0004-637X/747/1/35](https://doi.org/10.1088/0004-637X/747/1/35)
- Borucki, W. J., Koch, D., Basri, G., et al. 2010, *Science*, 327, 977, doi: [10.1126/science.1185402](https://doi.org/10.1126/science.1185402)
- Claret, A. 2018, *A&A*, 618, A20, doi: [10.1051/0004-6361/201833060](https://doi.org/10.1051/0004-6361/201833060)
- Delrez, L., Santerne, A., Almenara, J.-M., et al. 2016, *MNRAS*, 458, 4025, doi: [10.1093/mnras/stw522](https://doi.org/10.1093/mnras/stw522)
- Demangeon, O. D. S., Faedi, F., Hébrard, G., et al. 2018, *A&A*, 610, A63, doi: [10.1051/0004-6361/201731735](https://doi.org/10.1051/0004-6361/201731735)
- Deming, D., Wilkins, A., McCullough, P., et al. 2013, *ApJ*, 774, 95, doi: [10.1088/0004-637X/774/2/95](https://doi.org/10.1088/0004-637X/774/2/95)
- Drummond, B., Tremblin, P., Baraffe, I., et al. 2016, *A&A*, 594, A69, doi: [10.1051/0004-6361/201628799](https://doi.org/10.1051/0004-6361/201628799)
- Evans, T. M., Sing, D. K., Wakeford, H. R., et al. 2016, *ApJL*, 822, L4, doi: [10.3847/2041-8205/822/1/L4](https://doi.org/10.3847/2041-8205/822/1/L4)
- Evans, T. M., Sing, D. K., Kataria, T., et al. 2017, *Nature*, 548, 58, doi: [10.1038/nature23266](https://doi.org/10.1038/nature23266)
- Evans, T. M., Sing, D. K., Goyal, J. M., et al. 2018, *AJ*, 156, 283, doi: [10.3847/1538-3881/aaebff](https://doi.org/10.3847/1538-3881/aaebff)
- Gaia Collaboration, Brown, A. G. A., Vallenari, A., et al. 2016, *A&A*, 595, A2, doi: [10.1051/0004-6361/201629512](https://doi.org/10.1051/0004-6361/201629512)
- . 2018, *A&A*, 616, A1, doi: [10.1051/0004-6361/201833051](https://doi.org/10.1051/0004-6361/201833051)
- Gibson, N. P., Aigrain, S., Roberts, S., et al. 2012, *MNRAS*, 419, 2683, doi: [10.1111/j.1365-2966.2011.19915.x](https://doi.org/10.1111/j.1365-2966.2011.19915.x)
- Goyal, J. M., Wakeford, H. R., Mayne, N. J., et al. 2019, *MNRAS*, 482, 4503, doi: [10.1093/mnras/sty3001](https://doi.org/10.1093/mnras/sty3001)
- Goyal, J. M., Mayne, N., Sing, D. K., et al. 2018, *MNRAS*, 474, 5158, doi: [10.1093/mnras/stx3015](https://doi.org/10.1093/mnras/stx3015)
- Hogg, D. W., & Foreman-Mackey, D. 2018, *ApJS*, 236, 11, doi: [10.3847/1538-4365/aab76e](https://doi.org/10.3847/1538-4365/aab76e)
- Kipping, D. M. 2010, *MNRAS*, 408, 1758, doi: [10.1111/j.1365-2966.2010.17242.x](https://doi.org/10.1111/j.1365-2966.2010.17242.x)
- MacKay, D. J. C. 2002, *Information Theory, Inference & Learning Algorithms* (New York, NY, USA: Cambridge University Press)
- Madhusudhan, N., Harrington, J., Stevenson, K. B., et al. 2011, *Nature*, 469, 64, doi: [10.1038/nature09602](https://doi.org/10.1038/nature09602)
- Mandel, K., & Agol, E. 2002, *ApJ*, 580, L171, doi: [10.1086/345520](https://doi.org/10.1086/345520)
- Patil, A., Huard, D., & Fonnesbeck, C. J. 2010, *J. Stat. Softw.*, 1
- Pont, F., Knutson, H., Gilliland, R. L., Moutou, C., & Charbonneau, D. 2008, *MNRAS*, 385, 109, doi: [10.1111/j.1365-2966.2008.12852.x](https://doi.org/10.1111/j.1365-2966.2008.12852.x)
- Pukelsheim, F. 1994, *The American Statistician*, 48, 88, doi: [10.1080/00031305.1994.10476030](https://doi.org/10.1080/00031305.1994.10476030)
- Ricker, G. R., Winn, J. N., Vanderspek, R., et al. 2015a, *Journal of Astronomical Telescopes, Instruments, and Systems*, 1, 014003, doi: [10.1117/1.JATIS.1.1.014003](https://doi.org/10.1117/1.JATIS.1.1.014003)
- . 2015b, *Journal of Astronomical Telescopes, Instruments, and Systems*, 1, 014003, doi: [10.1117/1.JATIS.1.1.014003](https://doi.org/10.1117/1.JATIS.1.1.014003)
- Seager, S., & Deming, D. 2010, *ARA&A*, 48, 631, doi: [10.1146/annurev-astro-081309-130837](https://doi.org/10.1146/annurev-astro-081309-130837)
- Sing, D. K., Pont, F., Aigrain, S., et al. 2011, *MNRAS*, 416, 1443, doi: [10.1111/j.1365-2966.2011.19142.x](https://doi.org/10.1111/j.1365-2966.2011.19142.x)
- Sing, D. K., Fortney, J. J., Nikolov, N., et al. 2016, *Nature*, 529, 59, doi: [10.1038/nature16068](https://doi.org/10.1038/nature16068)
- Siverd, R. J., Collins, K. A., Zhou, G., et al. 2018, *AJ*, 155, 35, doi: [10.3847/1538-3881/aa9e4d](https://doi.org/10.3847/1538-3881/aa9e4d)
- Smith, J. C., Stumpe, M. C., Van Cleve, J. E., et al. 2012, *PASP*, 124, 1000, doi: [10.1086/667697](https://doi.org/10.1086/667697)
- Tremblin, P., Amundsen, D. S., Chabrier, G., et al. 2016, *ApJL*, 817, L19, doi: [10.3847/2041-8205/817/2/L19](https://doi.org/10.3847/2041-8205/817/2/L19)
- Tremblin, P., Amundsen, D. S., Mourier, P., et al. 2015, *ApJL*, 804, L17, doi: [10.1088/2041-8205/804/1/L17](https://doi.org/10.1088/2041-8205/804/1/L17)
- Vanderburg, A., & Johnson, J. A. 2014, *PASP*, 126, 948, doi: [10.1086/678764](https://doi.org/10.1086/678764)
- Vidal-Madjar, A., Lecavelier des Etangs, A., Désert, J. M., et al. 2003, *Nature*, 422, 143, doi: [10.1038/nature01448](https://doi.org/10.1038/nature01448)